Chiral Ligand-Induced Structural Transformation of Low-Dimensional Hybrid Perovskite for Circularly Polarized Photodetection

Journal:	*Chemistry of Materials*
Manuscript ID	cm-2021-03622p.R1
Manuscript Type:	Article
Date Submitted by the Author:	n/a
Complete List of Authors:	Li, Maoxin; Shenzhen University, Institute of Microscale Optoelectronics Fang, Feier; Shenzhen University, College of Electronics and Information Engineering Huang, Xiao; Shenzhen University Liu, Guangyou; Shenzhen University Lai, Zheng; Shenzhen University Chen, Zhihao; Shenzhen University Hong, Jiahao; Shenzhen University, Institute of Microscale Optoelectronics Chen, Yu; Shenzhen University, ICL 2DMOST Wei, Rong-Jia; Jinan University, Ning, Guo-Hong; Jinan Univeristy, College of Chemistry and Materials Science Leng, Kai; The Hong Kong Polytechnic University, Department of Applied Physics Shi, Yumeng; Shenzhen University, College of Electronics and Information Engineering Tian, Bingbing; Shenzhen University, Institute of Microscale Optoelectronics

Chiral Ligand-Induced Structural Transformation of Low-Dimensional Hybrid Perovskite for Circularly Polarized Photodetection

Maoxin Li,[a,#] Feier Fang[b,#], Xiao Huang,[a] Guangyou Liu,[a] Zheng Lai,[a] Zhihao Chen,[a] Jiahao Hong,[a] Yu Chen,[a] Rongjia Wei,[d] Guo-Hong Ning,[d] Kai Leng,[*,c] Yumeng Shi,[*,b], Bingbing Tian[*,a]

[a] *SZU-NUS Collaborative Innovation Center for Optoelectronic Science & Technology, International Collaborative Laboratory of 2D Materials for Optoelectronics Science and Technology of Ministry of Education, Institute of Microscale Optoelectronics, Shenzhen University, Shenzhen 518060, China*

[b] *College of Electronics and Information Engineering, Shenzhen University, Shenzhen 518060, China*

[c] *Department of Applied Physics, The Hong Kong Polytechnic University, Hung Hom, Kowloon, Hong Kong, China*

[d] *College of Chemistry and Materials Science, Guangdong Provincial Key Laboratory of Functional Supramolecular Coordination Materials and Applications, Jinan University, Guangzhou, Guangdong 510632, China*

[*] Email: kathy-kai.leng@polyu.edu.hk, yumeng.shi@szu.edu.cn, tianbb2011@szu.edu.cn

[#] These authors contributed equally

ABSTRACT: Chiral organic-inorganic hybrid perovskites (OIHPs) are inversion asymmetric and have many remarkable properties, including circular dichroism (CD), optical rotation, nonlinear optics, and second-harmonic generation (SHG). While chiral molecules are responsible for chiroptical properties, they are generally not expected to influence the crystallization of OIHPs. Here, we find that OIHPs synthesized with pristine S- and R-molecules crystallize as 1D perovskites, whereas that synthesized with the racemic molecule crystallized as 2D perovskites. Single crystal X-ray diffraction reveals that the structure change is related to the differing packing of chiral molecules versus racemic ones in OIHP. Furthermore, we demonstrate chiral OIHPs containing the S- or R-ligands could be applied in circularly polarized light (CPL) detectors.

KEYWORDS: chiral perovskite, single crystal, structure analysis, lattice parameter, CPL detection

INTRODUCTION

Organic-inorganic hybrid perovskites (OIHPs) have attracted great interest due to their excellent optoelectronic properties, including long carrier-diffusion lengths, low trap densities, high absorption coefficients, and tunable bandgaps.[1-3] These properties enable superior performance in solar cells,[4, 5] photodetectors,[6-8] and light-emitting diodes (LEDs).[9] Given the flexibility of the organic ligands in OIHPs, the introduction of chirality has produced a new subclass: chiral OIHPs.[10] Chiral OIHPs exhibit intriguing properties such as circular dichroism (CD), nonlinear optics, and ferroelectricity,[11] which can be potentially used in CPL sources,[12] circularly polarized photodetectors,[13] spintronics devices,[14] and ferroelectric materials.[15] In recent years, the introduction of structural asymmetry by using chiral organic groups have attracted a lot of attention. For instance, due to the non-centrosymmetric structures, chiral OIHPs are promising ferroelectric materials.[15-20] In addition, the coupling of structural asymmetry to spin-orbit coupling in chiral OIHPs may create Rashba-type spin polarization.[14, 21, 22] Owing to helicity-dependent excitons, OIHPs encompass the potential to be applied in circularly polarized light-emitting diode (CP-LED).[17, 23-26] CPL detection is a key to some critical applications, such as drug screening, security surveillance, and quantum optics.[13] Conventional CPL detectors require complex integration of components. Therefore, it is significant to explore materials sensitive to circularly polarized light. Tang et al. introduced R/S-α-phenylethylamine two-dimensional chiral OIHPs for a fast, atmospheric chiral photodetector.[13] Furthermore, different from pristine chiral OIHPs, Li's group usually utilized other materials forming heterojunctions with OIHPs to improve detection performance.[27, 28]

Generally, most studies on chiral OIHPs were focused on helicity-dependent exciton physics or spin-filtering, but few studies investigated if the crystal structures are affected by the chiral ligands.[29] In principle, chiral perovskites with same structure chiral ligands can be obtained by the same synthesis method.[15, 30] However, in many cases, racemic single crystals could not be crystallized in the same

crystal phase. A detail analysis of the packing of the organic ligands in chiral and racemic crystals is needed to explain this but is currently lacking.[13]

In this work, chiral OIHP crystals named (R/S-NEA)PbI_3 and (rac-NEA)$_2PbI_4$ with chiral ligands (R-(+)-/S-(−)-1-(2-naphthyl)ethylamine (R/S-NEA), or 1-(2-naphthyl)ethylamine (rac-NEA)) were synthesized by a facile solution method. The crystal structures of (R/S-NEA)PbI_3 and (rac-NEA)$_2PbI_4$ were solved by single crystal XRD. The UV-visible light absorption spectra and CD spectra confirm the chirality of the R and S-OIHP crystals. Second-harmonic generation (SHG) shows that the R- and S- OIHPs possess non-centrosymmetric structures and exhibit frequency multiplication. Diagrams of the unit cell structures were used to elucidate the growth behavior and phase difference in chiral crystals. Consequently, (R-NEA)PbI_3 and (S-NEA)PbI_3 present opposite photoelectric responses under CPL. Under the same power density, anisotropy factor for photocurrent of (R-NEA)PbI_3 and (S-NEA)PbI_3 detectors have been determined to be 0.294 and 0.24.

EXPERIMENTAL DETAILS

Materials. (S)-(−)-1-(2-naphthyl) ethylamine (≥98%) and (R)-(+)-1-(2-naphthyl) ethylamine (≥98%) were purchased from Tokyo Chemical Industry, and 1-(2-naphthyl) ethylamine (≥98%) was purchased from MERYER. Hydroiodic acid (HI) (55.0-58.0 wt.% in H_2O, containing≤1.5% H_3PO_2 stabilizer) was got from Aladdin and 1-Butanol (99.5%) were purchased from Energy Chemical. All reagents were used without further purification.

Synthesis. PbO (100.1 mg) was dissolved in a 58 wt.% HI solution (1.5 ml) contained in a pressurized vessel. A light brown solution was obtained after ultrasonication. R/S/rac-NEA (134.4 mg) and 1-Butanol (1 ml) were successively and slowly added dropwise into the pressure bottle. Then, the vessel was transferred to an oil bath held at 110 °C and heated until a bright yellow solution formed. Then the vessel was placed still under 110 °C for 6 h. Yellow crystals were obtained after the solution

was cooled down to 70 °C at a rate of 5 °C h^{-1} and then to 20 °C at a rate of 2 °C h^{-1}. The synthesis process of chiral OIHPs was shown in scheme S1. The crystals were filtered and then dried under a vacuum for one night.

Films fabrication. Perovskite films were prepared on either soda-lime glass (1.5×1.5 cm^2) or quartz glass (2×2 cm^2). The substrates were ultrasonically cleaned with deionized water, isopropanol, acetone; each cleaning step was performed over approximately 10 min. Then, the substrates were cleaned with oxygen plasma for 5 min. A chiral perovskite precursor solution (40 wt.% in DMF, 40 μL) was dispersed dropwise onto the substrates for spin-coating, and the samples were then spun at 2000 rpm for 30 s. Finally, the films were annealed at 120 °C for 8 min on a hot plate to induce crystallization. All processes were carried out in an argon-filled glove box.

Device fabrication. The chiral pristine perovskite devices were fabricated on sapphire substrates. Firstly, the chiral layered perovskites were exfoliated onto the substrate.[31] Subsequently, Au electrodes were deposited on the exfoliated flake by thermal evaporation to form a typical channel length of about 20 μm.

Characterization of the 2D hybrid perovskites. The morphologies of the prepared crystals and films were observed with scanning electron microscopy (SEM) (MIRA3, TESCAN). The structures of the crystals were characterized by X-ray diffraction (XRD) (Ultima IV, Rigaku) with a scanning speed of 4 ° min^{-1} at 40 kV and 40 mV. The arrangement of organic molecules and PbI_6 octahedra was determined by single-crystal XRD (Rigaku, Japan, Cu Kα, λ = 1.54178 Å). Structural symmetry and nonlinear data were obtained from SHG. CD measurements and UV-visible optical absorption spectra were obtained with a JASCO950 CD spectrometer over a range of 300-600 nm. The *I-V* curves were measured by Keithley 2600B SourceMeter SMU. The temporal voltage response to a pulsed light source was tested by a DMM7510 7½-bit graphic sampling multimeter. And the noise current of devices was recorded by a phase-locked amplifier SR830 (Stanford Research Systems).

RESULTS AND DISCUSSION

To verify the successful introduction of chirality into OIHPs, chiral perovskite crystals were prepared into thin films via spin-coating. **Figure 1c** shows digital and SEM images of the uniform films obtained. The XRD patterns of OIHPs films are shown in **Figure 1a**. Chiral OIHPs exhibit high crystallinity and oriented growth, and no impurity peaks were detected. XRD pattern indicates that the (0 0 *l*) planes of the crystals are parallel to the substrates, suggesting a high degree of orientation. (R-NEA)PbI_3 and (S-NEA)PbI_3 exhibit the same position of XRD peaks without any shifts. However, the main peak for (rac-NEA)$_2PbI_4$ shifts from 7.14° to 5.64° (~1.5°) compared to (R-NEA)PbI_3 and (S-NEA)PbI_3. Thus, (rac-NEA)$_2PbI_4$ exhibits a larger interlayer spacing.

Figure 1b shows the CD spectra and UV absorption spectra of the three perovskite films. The CD spectra indicate that the R- and S- configured chiral organic cations were successfully introduced into the perovskites, exhibiting optical chirality. The chiral molecules R/S/rac-NEA were dissolved in 1-butanol, then the CD spectra of chiral ligands were measured and shown in **Figure S1**, which are different from chiral perovskites. When a beam of linearly polarized light passes through the perovskite films, (R-NEA)PbI_3 and (S-NEA)PbI_3 absorbed left and right CPL at different rates. In contrast to most other reported perovskites, (R-NEA)PbI_3 and (S-NEA)PbI_3 exhibit strong chiral optical activity.[32, 33] In **Figure 1b**, the peaks of (R-NEA)PbI_3 and (S-NEA)PbI_3 are observed at 370 nm and extrapolated to 397 nm. The UV spectrum of (rac-NEA)$_2PbI_4$ was located at 412 nm and extrapolated to 435nm. The narrow bandwidth peak located at 370 nm and 412nm are attributed to exciton of (S/R-NEA)PbI_3 crystals.[34] A platform is located at 385nm in the UV spectrum of (rac-NEA)$_2PbI_4$ which can be attributed to higher energy electronic bands.[3] The optical band gaps were calculated according to the absorption spectra. The values of band gaps for (S/R-NEA)PbI_3 and (rac-NEA)$_2PbI_4$ are 3.20 and 2.90 eV, respectively (**Figure S2**). The UV spectra reveal that the CD peaks are slightly red-shifted to the extinction band edge. The wavelength corresponding to the intersection of the CD spectral curve and

the zero line match with the extinction band edge of the sample. This phenomenon is known as the Cotton effect, which is caused by the energy level splitting of the related electronic states of a semiconductor due to the chiral organic ligands.[35] The (rac-NEA)$_2$PbI$_4$ shows no chiral optical activity, but its UV spectrum is redshifted compared to that of (R-NEA)PbI$_3$ and (S-NEA)PbI$_3$. This can be attributed to the different assembly manner of the $(PbI_6)^{4-}$ octahedra.[36] In the OIHPs with the same organic ligands, the absorption band of corner-sharing $(PbI_6)^{4-}$ octahedra is wider than that of face-sharing $(PbI_6)^{4-}$ octahedra.[37] The lack of inversion symmetry of the chiral compound can be proven by the ability to generate SHG response (**Figure 1d**). Under 800nm incident laser, (R-NEA)PbI$_3$ and (S-NEA)PbI$_3$ are SHG-active while (rac-NEA)$_2$PbI$_4$ is inactive. Furthermore, there was no noticeable differences were observed among the XRD spectra of as-prepared, 3-day-, 7-day-, 15-day-aged films (**Figure S3**). It indicates that films have good stability.

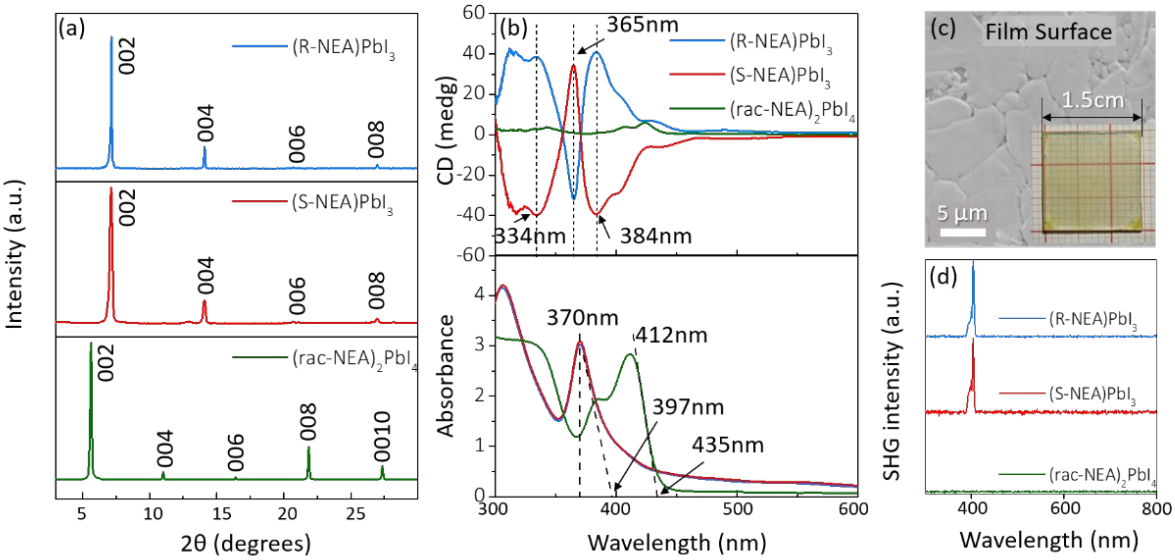

Figure 1. Characterization of the chiral perovskite films. (a) XRD patterns of the (R-/S-NEA)PbI$_3$ films and (rac-NEA)$_2$PbI$_4$. (b) CD and absorption of the highly oriented films. (c) Digital and SEM images of a film. (d) Wavelength-dependent SHG singles of the films.

Figure 2 shows digital images, XRD patterns, and X-ray oscillation photographs of the chiral OIHPs single crystals. In this case, R-/S-/rac-NEA reacted with PbO in an HI solution under ambient atmospheric conditions, and block-shaped, yellow single crystals with millimeter-scale to the

centimeter scale were got by regulating the cooling rate (**Figure 2a**). **Figure 2b** shows the small, block-shaped (S-NEA)PbI_3 single crystals obtained (for (R-NEA)PbI_3 and (rac-NEA)$_2PbI_4$ see **Figure S4**). **Figure 2c** presents XRD patterns of the (R-/S-NEA)PbI_3 and (rac-NEA)$_2PbI_4$ crystals. The main peaks corresponding to (R-/S-NEA)PbI_3 and (rac-NEA)$_2PbI_4$ are consistent with those observed in the XRD patterns of the films. **Figure 2d** and 2e show single-crystal X-ray oscillation photographs of (R-NEA)PbI_3 and (rac-NEA)$_2PbI_4$. The main Bragg reflections can be observed in the photographs, and the structure of the crystals was analyzed using single-crystal X-ray intensity data.

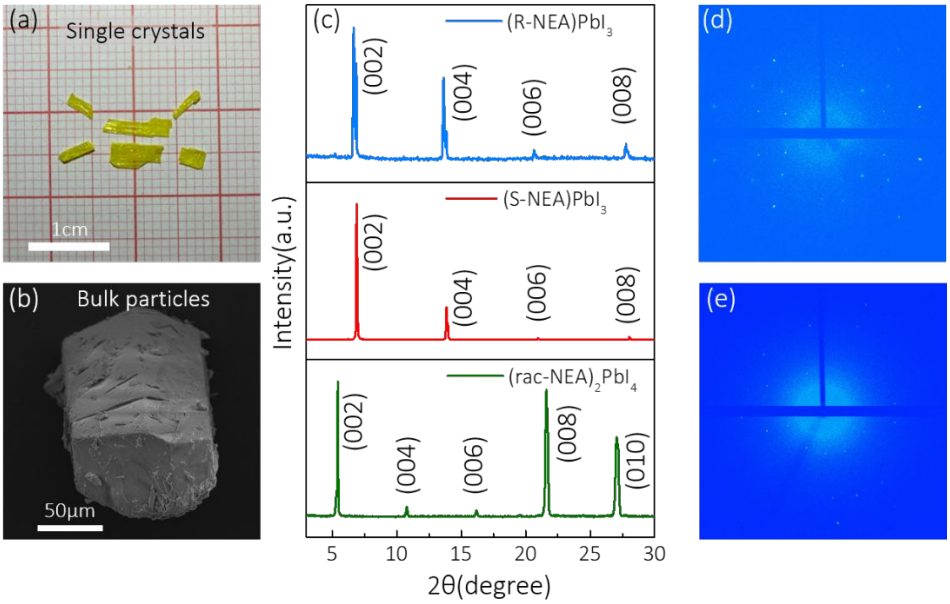

Figure 2. Characterization of the chiral perovskite single crystals. (a) Digital photograph of the single crystals. (b) SEM image of (S-NEA)PbI_3. (c) XRD patterns of the (R-/S-NEA)PbI_3 and (rac-NEA)$_2PbI_4$ crystals. Single-crystal X-ray oscillation photographs of (d) (R-NEA)PbI_3 and (e) (rac-NEA)$_2PbI_4$.

The single-crystal structures of (R-/S-NEA)PbI_3 and (rac-NEA)$_2PbI_4$ were deciphered and schemes of the crystalline structures are shown in **Figure 3**. The chiral OIHPs investigated in this paper can be described as low-dimensional hybrid perovskite structures.[38] As shown in the schematic, there are some differences among the layered structures of (R-/S-NEA)PbI_3 and (rac-NEA)$_2PbI_4$. In the two chiral perovskites, the structures consist of face-sharing $(PbI_6)^{4-}$ octahedral layers separated by

R/S organic ligands (**Figure 3a**, **3b**). In the absence of the simulated octahedra, the iodine atoms are arranged in a spiral around the lead atoms, and every iodine atom is connected to a hydrogen atom in the -NH_2 group. The chains of the inorganic layer are formed by three bridging halides with shared faces. In the achiral compound, the structure consists of corner-sharing $(PbI_6)^{4-}$ octahedra layers and a racemic organic layer (**Figure 3**). Hydrogen bonding exists between the ends of the organic molecules and halide atoms. The bulky cations interact with the inorganic cages via hydrogen bonding. Based on the theory of preferential growth in crystallography,[39] orthorhombic (R-/S-NEA)PbI_3 and triclinic (rac-NEA)$_2PbI_4$ were synthesized.[29] R-/S-NEA organic ligands are regularly distributed on both sides of the inorganic chains but the organic molecules are mirror images seen from the A axis (**Figure S5**). In (rac-NEA)$_2PbI_4$, each halogen atom is shared by two octahedra that are connected to form an inorganic layer. The amine group on each rac-NEA unit forms hydrogen bonds with the nearest octahedron to achieve stability. More detailed information of (R-NEA)PbI_3 and (rac-NEA)$_2PbI_4$ are shown in **Figure S6** and **Figure S7**.

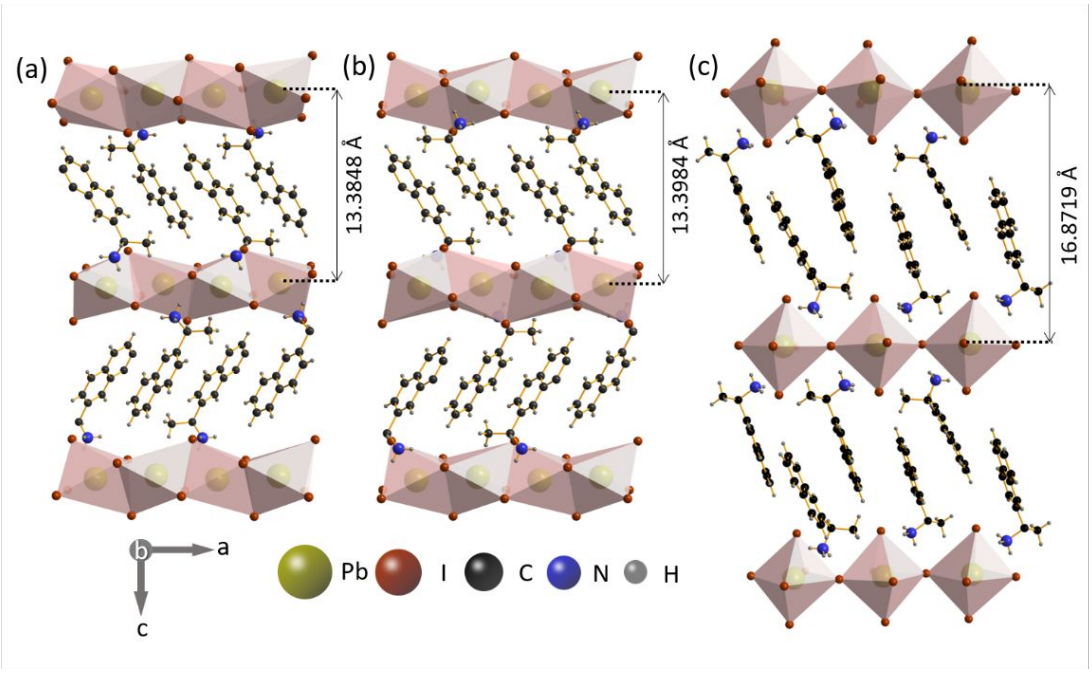

Figure 3. Packing views of the crystal structures of (a) (S-NEA)PbI_3, (b) (R-NEA)PbI_3, (c) (rac-NEA)$_2PbI_4$.

Additional crystallographic data are summarized in Table 1. At 298 K, (R-/S-NEA)PbI_3 crystallizes in the P_{212121} space group, which is included in the 65 Sohncke chiral space groups listed, and (rac-NEA)$_2PbI_4$ crystallizes in the $P\bar{1}$ space group. Under the same facile solution synthesis conditions, the rotation of the organic ligands determined the hydrogen bonds between the amines and halogen atoms. The atomic coordinates and equivalent displacement parameters of (R-/S-NEA)PbI_3 and (rac-NEA)$_2PbI_4$ are shown in Table S1-S3. And CCDC reference numbers are 2116341-2116343. The unit compounds of (R-/S-NEA)PbI_3 and (rac-NEA)$_2PbI_4$ are shown in **Figure S16**.

Table 1. Summary of the crystal data and structure refinements of (R-/S-NEA)PbI_3 and (rac-NEA)$_2PbI_4$.

	(S-NEA)PbI_3	(R-NEA)PbI_3	(rac-NEA)$_2PbI_4$
Empirical formula	$C_{12}H_{14}NPbI_3$	$C_{12}H_{14}NPbI_3$	$(C_{12}H_{14}N)_2PbI_4$
Temperature (K)	298 K	298K	100K
Wavelength (Å)	1.54184	1.54184	1.54184
Crystal color	Yellow	Yellow	Yellow
Crystal system	Orthorhombic	Orthorhombic	Triclinic
Space group	No.19 ($P_{2_12_12_1}$)	No. 19 ($P_{2_12_12_1}$)	No.2 ($P\bar{1}$)
a (Å)	8.1587(3)	8.1576(1)	8.8362(2)
b (Å)	8.5685(2)	8.5778(1)	16.8772(5)
c (Å)	25.4809(8)	25.5061(2)	19.6117(4)
α (°)	90	90	93.564
β (°)	90	90	100.851
γ (°)	90	90	100.632
Volume (Å^3)	1781.31(10)	1784.77(3)	2808.79(12)
Z	4	4	1
Density (g cm^{-3})	2.834	2.829	2.251
M (mm^{-1})	59.094	58.979	39.159
F (000)	1336	1336	1747
Theta (max)	77.666	77.615	64.999
Data completeness	1.64/0.95	1.66/0.96	0.985
R (reflections)	0.0970(3441)	0.0474(3517)	0.0450 (7609)
wR2 (reflections)	0.2507(3595)	0.1148(3645)	0.1160 (9410)
No. of parameters	132	156	625
S	1.153	1.075	1.048

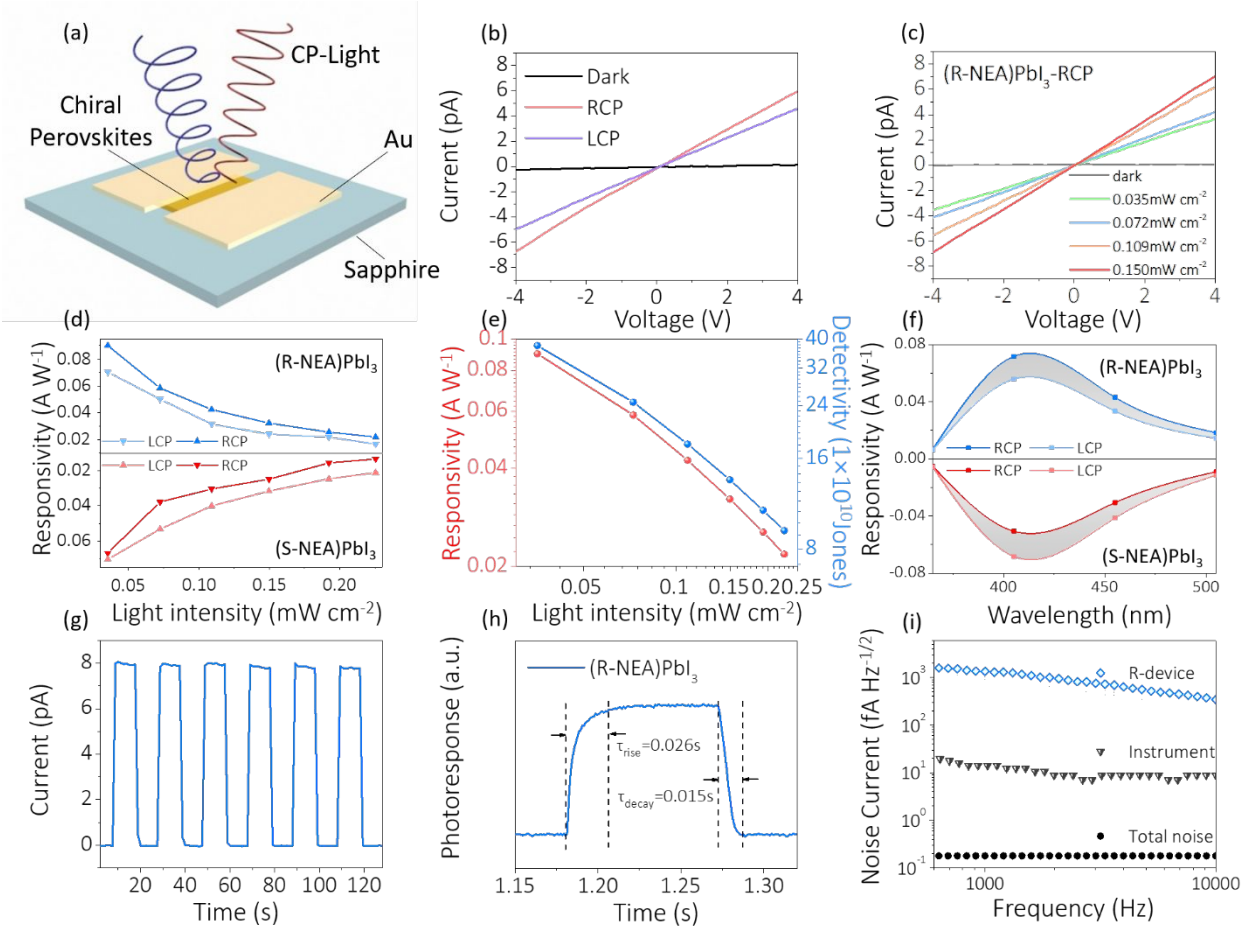

Figure 4. The device performance of (R-NEA)PbI_3 CPL detectors. (a) Schematic diagram of CPL detector. (b) The current-voltage (I-V) curves of the device under dark, RCP-405nm, and LCP-405nm light illumination. (c) The I-V curves under different light power densities (ranging from 0 to 0.15 mW cm^{-2}). (d) Spectral response of (R-NEA)PbI_3 and (S-NEA)PbI_3 devices under CPL illumination with different light power densities. (e) *R* and detectivity (D^*) as a function of the incident light power density. (f) The responsivity of (R-/S-NEA)PbI_3 device under LCP and RCP light at the wavelengths of 365, 405, 455, and 505 nm. (g) Photoresponse under cyclic light illumination. (h) Temporal voltage response to a pulsed light source. (i) Noise current spectra of the device, instrument, and the total noise.

A chiral OIHP thin flake can be mechanically exfoliated from bulk crystals due to the relatively weak van der Waals forces between the organic chains of two unit cells.[40] As shown in **Figure 4a**, chiral OIHPs photodetectors were successfully fabricated with a channel length of 20 μm. The corresponding OM image of a typical photodetector is shown in **Figure S8**. The thickness of the mechanically exfoliated flakes was obtained by Atomic Force Microscope (AFM). The thicknesses of

(R-NEA)PbI_3, (S-NEA)PbI_3 and (rac-NEA)$_2PbI_4$ flakes are 75.3, 76.4 and 72.4 nm, respectively (**Figure S9**). The device can detect CPL at room temperature and exhibit a high photoelectric detection performance. CPL was assembled by a 405nm laser, a linear polarizer, and a quarter-wave plate. **Figure 4b** shows the I-V curves of the (R-NEA)PbI_3 CPL detectors in the dark and under right-handed circular polarized (RCP), and left-handed circular polarized (LCP) illumination. Obviously, (R-NEA)PbI_3 CPL detectors exhibit a higher photocurrent under RCP illumination compared with that under LCP illumination. Impressively, (S-NEA)PbI_3 devices exhibit an opposite trend (**Figure S11a**), indicating distinguishing ability for RCP and LCP illumination. Under a bias of 0.4 V, the dark current is 2.82×10^{-2} pA, the photocurrent of (R-NEA)PbI_3 photodetector can reach 1.4 pA under a power density of 0.15 mW cm^{-2}, and a maximum on/off ratio is about 117. The anisotropy factor for photocurrent can be defined as $g_{Iph} = 2 \mid (I_R-I_L)/(I_R+I_L) \mid$, where I_R and I_L are the photocurrents under RCP and LCP illumination, respectively.[27, 41-43] This parameter represents the degree of CPL detection capability. Under the 405nm-CPL with a power density of 0.15 mW cm^{-2} and at a bias of 4 V, the g_{Iph} of (R-NEA)PbI_3 and (S-NEA)PbI_3 were calculated to be 0.294 and 0.24, respectively. Compared with other various CPL detectors based on pristine chiral OIHPs, (R-NEA)PbI_3 and (S-NEA)PbI_3 CPL detectors shows an excellent detection capability.[13, 28, 43] The photocurrents of (rac-NEA)$_2PbI_4$ CPL detectors under RCP and LCP illumination in **Figure S12a** are the same, as expected of a non-chiral compound with no helicity dependence.[44] The I-V curves of the three devices under dark conditions and different light power densities are shown in **Figure 4c** (**Figures S11b** and **S12b**). The linear dynamic range (LDR) can be calculated by LDR= 20 log Pmax/Pmin, where P_{max} and P_{min} are the maximum and minimum incident light power intensities in the linear range, respectively. The LDR of the CPL detector under CPL with light intensity ranging from 0.035 to 0.15 mW cm^{-2} is shown in **Figure S10**, indicating that LDR is ≈ 13dB. As the light power density increased from 0 to 0.15 mW cm^{-2}, the photocurrent gradually increases due to the number of photogenerated charge carriers is

directly proportional to the absorbed photon flux. The linear of I-V curves indicate that the Au electrodes formed ohmic contact on chiral perovskites. [45] The photocurrent and R of (R-NEA)PbI_3 photodetectors under various RCP light power densities with a bias of 5V as shown in **Figure S13**. The corresponding calculation equation is defined as follows:[45]

$$R = \frac{I_{light} - I_{dark}}{PA} \quad (1)$$

where I_{light} and I_{dark} mean photocurrent under 405nm-CPL and dark current respectively. P is the light power density and A is the active area of devices. The photocurrent increases continuously with the incident light power density, while the value of *R* decreases. This is attributed to the relative large recombination possibility of photogenerated carrier as the carrier density increases under high light power. (S-NEA)PbI_3 and (rac-NEA)$_2PbI_4$ also reached the saturation current under the same incident light intensity shown in **Figure S11c** and **Figure S12c**. Under incident light power density of 0.035 mW cm^{-2}, the highest *R* (0.09 A W^{-1}) was achieved. **Figure 4f** shows the wavelength-dependent (from 365-505 nm) R under 4V.

In **Figure 4d**, the *R* of the (R-NEA)PbI_3 and (S-NEA)PbI_3 devices exhibit a symmetrical trend under CPL illumination. The *R* of the two devices demonstrated that (R-NEA)PbI_3 was more responsive to RCP, while (S-NEA)PbI_3 exhibit the opposite phenomenon. **Figure 4e** exhibits the relationship between *R* and D^* for (R-NEA)PbI_3 CPL detectors as a function of incident light power density, respectively. In addition, D^* is also an important parameter describing the performance of a detector. D^* can be calculated as follows:

$$D^* = \frac{(A\Delta f_x)^{1/2}}{NEP} \quad (2)$$

$$NEP = \frac{i_{noise}}{R} \quad (3)$$

where *R* is responsivity, Δf_x is the bandwidth of the equipment (0.833 Hz), NEP is the noise-equivalent power. The value of shot noise (2.94×10^{-1} fA $Hz^{-1/2}$) is more than 10 times larger than that of the thermal noise (1.73×10^{-2} fA $Hz^{-1/2}$), therefore the total noise current in our devices can be

dominated by the shot noise (**Figure 4i**):

$$i_{noise} \approx \sqrt{2eI_d\Delta f_x} \quad (4)$$

D^* can be expressed as

$$D^* = \sqrt{\frac{A}{2eI_d}}R \quad (5)$$

where e is the elementary charge, I_d is the dark current. Using these equations above, the maximum D^* reached about 3.8×10^{11} Jones with the light power intensity of 0.035 mW cm^{-2}. Table 2 lists the corresponding comparison performance of CPL photodetectors based on chiral perovskites.[13, 27, 28, 43, 46-48] Compared with previously reported CPL devices, the photodetector based on 1D (R/S-NEA)PbI_3 show some superior properties such as D^* and g_{Iph} value.

Table 2. Summary of the CPL photodetectors performances

Materials	P_{inc} (mW cm^{-2})	Channel length (μm)	R (A W^{-1})	D^* (Jones)	Response time (ms)	On/off ratio	CD (medg)	g_{Iph}	Ref.
(R/S-α-PEA)PbI_3	0.252	-	0.797	7.1×10^{11}	-	-	180	0.1	13
hBN/(R/S-MBA)$_2PbI_4$/MoS_2	1.25	10	0.45	2.2×10^{11}	104	14	-	-	27
(R/S-α-PEA)$_2PbI_4$	0.00234	20	0.6	3.06×10^{11}	22	124	50	0.23	28
(R/S-MPA)$_4AgBiI_8$	270	-	22×10^{-6}	1.2×10^{7}	580	-	-	0.22	43
(R/S-β-MPA)$_2MAPb_2I_7$	0.23	-	3.8	1.1×10^{12}	1.6	-	30	0.2	46
(R/S-BPEA)$_2PbI_4$	150	-	0.0021	3×10^{11}	0.242	2×10^4	130	-	47
(R/S-MPA)$_2MAPb_2I_7$/$MAPbI_3$	0.2	-	0.0012	1.1×10^{12}	2	10^5	12	0.67	48
(R/S-NEA)PbI_3	0.035	20	0.09	3.8×10^{11}	26	117	40	0.294	This work

The time-dependent photocurrent response and the time response of (R-NEA)PbI_3 are shown in **Figure 4g**, 4h, respectively. To examine the stability of chiral perovskites detectors, on/off switching behavior of R-NEA)PbI_3 detectors remained stable for multiple cycles, as shown in **Figure 4g**. We further investigated the response time of (R-NEA)PbI_3 detectors, the rise and decay time of the device are 0.026s/0.015s, as shown in **Figure 4h**.

CONCLUSIONS

In summary, a class of chiral OIHP single crystals was successfully synthesized by a facile

solution method. Both CD and UV spectra proved that chirality has been successfully introduced into the organic ligands. XRD reveal that (R-/S-NEA)PbI_3 and (rac-NEA)$_2PbI_4$ have different crystal structures owing to the different packing geometry of the organic ligands. Finally, CPL detectors based on these chiral OIHPs achieved 0.294 anisotropy photocurrent and an R of 90 mA W^{-1}. The devices exhibited a high D^* of 3.8×10^{11} Jones and a response time of 0.026 s. We believe this work provides the necessary guideline for discovering new chiral OIHPs for optoelectronics and spintronics applications.

■ ASSOCIATED CONTENT

Ⓢ Supporting Information

The Supporting Information is available free of charge at XXXX.

Schematic illustration of the synthesis process, XRD spectra, SEM images, crystal structures, OM image, photocurrent characteristics, device performances, noise current spectra of devices.

■ AUTHOR INFORMATION

Author Contributions

[#] M. Li and F. Fang contributed equally to this work. The manuscript was written through contributions of all of the authors. All of the authors have given approval to the final version of the manuscript.

Notes

The authors declare no competing financial interest.

■ ACKNOWLEDGMENTS

B.T. acknowledges the financial support from the Guangdong Natural Science Funds (2019A1515010675), the Science and Technology Project of Shenzhen (JCYJ20210324094206019). K.L. acknowledges the Research Grants Council of the Hong Kong Special Administrative Region, China (Project No. PolyU15305221 for GRF project funded in 2021/22 Exercise) and Project 12104382 supported by National Natural Science Foundation of China.

■ REFERENCES

(1) Cao, F.; Chen, J.; Yu, D.; Wang, S.; Xu, X.; Liu, J.; Han, Z.; Huang, B.; Cu, Y.; Choy, K. L.; Zeng, H. Bionic Detectors Based on Low-Bandgap Inorganic Perovskite for Selective NIR-I Photon Detection and Imaging. *Adv. Mater.* **2020,** *32*, 1905362.

(2) Yu, D.; Cao, F.; Gao, Y.; Xiong, Y.; Zeng, H. Room-Temperature Ion-Exchange-Mediated Self-Assembly toward Formamidinium Perovskite Nanoplates with Finely Tunable, Ultrapure Green Emissions for Achieving Rec. 2020 Displays. *Adv. Funct. Mater.* **2018,** *28*, 1800248.

(3) Yu, D. J.; Cao, F.; Gu, Y.; Han, Z. Y.; Liu, J. X.; Huang, B.; Xu, X. B.; Zeng, H. B. Broadband and sensitive two-dimensional halide perovskite photodetector for full-spectrum underwater optical communication. *Nano Res.* **2021,** *14*, 1210-1217.

(4) Duong, T.; Pham, H.; Kho, T. C.; Phang, P.; Fong, K. C.; Yan, D.; Yin, Y. T.; Peng, J.; Mahmud, M. A.; Gharibzadeh, S.; Nejand, B. A.; Hossain, I. M.; Khan, M. R.; Mozaffari, N.; Wu, Y. L.; Shen, H. P.; Zheng, J. H.; Mai, H. X.; Liang, W. S.; Samundsett, C.; Stocks, M.; McIntosh, K.; Andersson, G. G.; Lemmer, U.; Richards, B. S.; Paetzold, U. W.; Ho-Ballie, A.; Liu, Y.; Macdonald, D.; Blakers, A.; Wong-Leung, J.; White, T.; Weber, K.; Catchpole, K. High Efficiency Perovskite-Silicon Tandem Solar Cells: Effect of Surface Coating versus Bulk Incorporation of 2D Perovskite. *Adv. Energy Mater.* **2020,** *10*, 1903553.

(5) Lin, Y. H.; Sakai, N.; Da, P.; Wu, J. Y.; Sansom, H. C.; Ramadan, A. J.; Mahesh, S.; Liu, J. L.; Oliver, R. D. J.; Lim, J.; Aspitarte, L.; Sharma, K.; Madhu, P. K.; Morales-Vilches, A. B.; Nayak, P. K.; Bai, S.; Gao, F.; Grovenor, C. R. M.; Johnston, M. B.; Labram, J. G.; Durrant, J. R.; Ball, J. M.; Wenger, B.; Stannowski, B.; Snaith, H. J. A piperidinium salt stabilizes efficient metal-halide perovskite solar cells. *Science* **2020,** *369*, 96-102.

(6) Li, D.; Liu, X. T.; Wu, W. T.; Peng, Y.; Zhao, S. G.; Li, L. N.; Hong, M. C.; Luo, J. H. Chiral Lead-Free Hybrid Perovskites for Self-Powered Circularly Polarized Light Detection. *Angew. Chem. Int. Ed. Engl.* **2020,** *60*, 8415-8418.

(7) Yu, D.; Cai, B.; Cao, F.; Li, X.; Liu, X.; Zhu, Y.; Ji, J.; Gu, Y.; Zeng, H. Cation Exchange-Induced Dimensionality Construction: From Monolayered to Multilayered 2D Single Crystal Halide Perovskites. *Adv. Mater. Interfaces* **2017,** *4*, 1700441.

(8) Liu, G. Y.; Qiu, C. T.; Tian, B. B.; Pan, X. N.; Ding, D.; Chen, Y.; Ren, C.; He, T. C.; Shi, Y. M.; Su, C. L.; Li, Y.; Gao, Y. X.; Fan, D. Y. Influence of the Organic Chain on the Optical Properties of Two-Dimensional Organic-Inorganic Hybrid Lead Iodide Perovskites. *Acs Applied Electronic Materials* **2019,** *1*, 2253-2259.

(9) Kim, Y. H.; Cho, H.; Heo, J. H.; Kim, T. S.; Myoung, N.; Lee, C. L.; Im, S. H.; Lee, T. W. Multicolored Organic/Inorganic Hybrid Perovskite Light-Emitting Diodes. *Adv. Mater.* **2015,** *27*, 1248-1254.

(10) Lemmerer, A.; Billing, D. G. Inorganic-Organic Hybrids Incorporating a Chiral Cyclic Ammonium Cation. *CrystEngComm* **2006,** *8*, 686-695.

(11) Long, G.; Sabatini, R.; Saidaminov, M. I.; Lakhwani, G.; Rasmita, A.; Liu, X.; Sargent, E. H.; Gao, W. Chiral-perovskite optoelectronics. *Nat. Rev. Mater.* **2020,** *5*, 423-439.

(12) Di Nuzzo, D.; Cui, L.; Greenfield, J. L.; Zhao, B.; Friend, R. H.; Meskers, S. C. J. Circularly Polarized Photoluminescence from Chiral Perovskite Thin Films at Room Temperature. *ACS Nano* **2020,** *14*, 7610-7616.

(13) Chen, C.; Gao, L.; Gao, W.; Ge, C.; Du, X.; Li, Z.; Yang, Y.; Niu, G.; Tang, J. Circularly polarized light detection using chiral hybrid perovskite. *Nat. Commun.* **2019,** *10*, 1927.

(14) Lu, H.; Wang, J.; Xiao, C.; Pan, X.; Chen, X.; Brunecky, R.; Berry, J. J.; Zhu, K.; Beard, M. C.; Vardeny, Z. V. Spin-dependent charge transport through 2D chiral hybrid lead-iodide perovskites. *Sci.*

Adv. **2019,** *5*, eaay0571.
(15) Yang, C. K.; Chen, W. N.; Ding, Y. T.; Wang, J.; Rao, Y.; Liao, W. Q.; Tang, Y. Y.; Li, P. F.; Wang, Z. X.; Xiong, R. G. The First 2D Homochiral Lead Iodide Perovskite Ferroelectrics: [R- and S-1-(4-Chlorophenyl)ethylammonium]$_2$PbI$_4$. *Adv. Mater.* **2019,** *31*, 1808088.
(16) Deng, B.-B.; Xu, C.-C.; Cheng, T.-T.; Yang, Y.-T.; Hu, Y.-T.; Wang, P.; He, W.-H.; Yang, M.-J.; Liao, W.-Q. Homochiral Nickel Nitrite ABX_3 ($X = NO^{2-}$) Perovskite Ferroelectrics. *J. Am. Chem. Soc.* **2020,** *142*, 6946-6950.
(17) Gao, J.-X.; Zhang, W.-Y.; Wu, Z.-G.; Zheng, Y.-X.; Fu, D.-W. Enantiomorphic Perovskite Ferroelectrics with Circularly Polarized Luminescence. *J. Am. Chem. Soc.* **2020,** *142*, 4756-4761.
(18) Hui, Y.; Florio, F.; Chen, Z.; Phelan, W. A.; Siegler, M. A.; Zhou, Z.; Guo, Y.; Hawks, R.; Jiang, J.; Feng, J.; Zhang, L.; Wang, B.; Wang, Y.; Gall, D.; Palermo, E. F.; Lu, Z.; Sun, X.; Lu, T.-M.; Zhou, H.; Ren, Y.; Wertz, E.; Sundararaman, R.; Shi, J. A chiral switchable photovoltaic ferroelectric 1D perovskite. *Sci. Adv.* **2020,** *6*, eaay4213.
(19) Shi, C.; Ye, L.; Gong, Z.-X.; Ma, J.-J.; Wang, Q.-W.; Jiang, J.-Y.; Hua, M.-M.; Wang, C.-F.; Yu, H.; Zhang, Y.; Ye, H.-Y. Two-Dimensional Organic-Inorganic Hybrid Rare-Earth Double Perovskite Ferroelectrics. *J. Am. Chem. Soc.* **2020,** *142*, 545-551.
(20) Shahrokhi, S.; Gao, W.; Wang, Y.; Anandan, P. R.; Rahaman, M. Z.; Singh, S.; Wang, D.; Cazorla, C.; Yuan, G.; Liu, J.-M.; Wu, T. Emergence of Ferroelectricity in Halide Perovskites. *Small Methods* **2020,** *4*.
(21) Huang, Z.; Bloom, B. P.; Ni, X.; Georgieva, Z. N.; Marciesky, M.; Vetter, E.; Liu, F.; Waldeck, D. H.; Sun, D. Magneto-Optical Detection of Photoinduced Magnetism via Chirality-Induced Spin Selectivity in 2D Chiral Hybrid Organic-Inorganic Perovskites. *ACS Nano* **2020,** *14*, 10370-10375.
(22) Jana, M. K.; Song, R.; Liu, H.; Khanal, D. R.; Janke, S. M.; Zhao, R.; Liu, C.; Valy Vardeny, Z.; Blum, V.; Mitzi, D. B. Organic-to-inorganic structural chirality transfer in a 2D hybrid perovskite and impact on Rashba-Dresselhaus spin-orbit coupling. *Nat. Commun.* **2020,** *11*, 4699-4699.
(23) Wang, C.-T.; Chen, K.; Xu, P.; Yeung, F.; Kwok, H.-S.; Li, G. Fully Chiral Light Emission from $CsPbX_3$ Perovskite Nanocrystals Enabled by Cholesteric Superstructure Stacks. *Adv. Funct. Mater.* **2019,** *29*, 1903155.
(24) Yang, X.; Zhou, M.; Wang, Y.; Duan, P. Electric-Field-Regulated Energy Transfer in Chiral Liquid Crystals for Enhancing Upconverted Circularly Polarized Luminescence through Steering the Photonic Bandgap. *Adv. Mater.* **2020,** *32*, 2000820.
(25) Li, Z.; Liu, H.; Li, F.; Zhao, J.; Wang, Y. Self-Assembly of Chiral Nematic Liquid Crystalline Phases of AgNR@SiO2@Cysteine@CsPbBr3 Hybrid Nanorods with Plasmon-Dependent Photoluminescence. *Particle & Particle Systems Characterization* **2020,** *37*, 2000008.
(26) Kim, Y.-H.; Zhai, Y.; Lu, H.; Pan, X.; Xiao, C.; Gaulding, E. A.; Harvey, S. P.; Berry, J. J.; Vardeny, Z. V.; Luther, J. M.; Beard, M. C. Chiral-induced spin selectivity enables a room-temperature spin light-emitting diode. *Science* **2021,** *371*, 1129-1133.
(27) Ma, J.; Fang, C.; Chen, C.; Jin, L.; Wang, J.; Wang, S.; Tang, J.; Li, D. Chiral 2D Perovskites with a High Degree of Circularly Polarized Photoluminescence. *ACS Nano* **2019,** *13*, 3659-3665.
(28) Wang, J.; Fang, C.; Ma, J.; Wang, S.; Jin, L.; Li, W.; Li, D. Aqueous Synthesis of Low-Dimensional Lead Halide Perovskites for Room-Temperature Circularly Polarized Light Emission and Detection. *ACS Nano* **2019,** *13*, 9473-9481.
(29) Dang, Y.; Liu, X.; Sun, Y.; Song, J.; Hu, W.; Tao, X. Bulk Chiral Halide Perovskite Single Crystals for Active Circular Dichroism and Circularly Polarized Luminescence. *J. Phys. Chem. Lett.* **2020,** *11*, 1689-1696.
(30) Ahn, J.; Ma, S.; Kim, J.-Y.; Kyhm, J.; Yang, W.; Lim, J. A.; Kotov, N. A.; Moon, J. Chiral 2D Organic Inorganic Hybrid Perovskite with Circular Dichroism Tunable Over Wide Wavelength Range. *J. Am. Chem. Soc.* **2020,** *142*, 4206-4212.

(31) Leng, K.; Abdelwahab, I.; Verzhbitskiy, I.; Telychko, M.; Chu, L. Q.; Fu, W.; Chi, X.; Guo, N.; Chen, Z. H.; Chen, Z. X.; Zhang, C.; Xu, Q. H.; Lu, J.; Chhowalla, M.; Eda, G.; Loh, K. P. Molecularly thin two-dimensional hybrid perovskites with tunable optoelectronic properties due to reversible surface relaxation. *Nat. Mater.* **2018,** *17*, 908-914.
(32) Georgieva, Z. N.; Bloom, B. P.; Ghosh, S.; Waldeck, D. H. Imprinting Chirality onto the Electronic States of Colloidal Perovskite Nanoplatelets. *Adv. Mater.* **2018,** *30*, 1800097.
(33) Peng, Y.; Yao, Y.; Li, L.; Wu, Z.; Wang, S.; Luo, J. White-light emission in a chiral one-dimensional organic-inorganic hybrid perovskite. *J. Mater. Chem. C* **2018,** *6*, 6033-6037.
(34) Mao, L. L.; Tsai, H.; Nie, W. Y.; Ma, L.; Im, J.; Stoumpos, C. C.; Malliakas, C. D.; Hao, F.; Wasielewski, M. R.; Mohite, A. D.; Kanatzidis, M. G. Role of Organic Counterion in Lead- and Tin-Based Two-Dimensional Semiconducting Iodide Perovskites and Application in Planar Solar Cells. *Chem. Mater.* **2016,** *28*, 7781-7792.
(35) Schellman, J. A.; Oriel, P. Origin of Cotton Effect of Helical Polypeptides. *J. Chem. Phys.* **1962,** *37*, 2114-2124.
(36) Rahaman, M. Z.; Ge, S.; Lin, C.-H.; Cui, Y.; Wu, T. One-Dimensional Molecular Metal Halide Materials: Structures, Properties, and Applications. *Small Structures* **2021,** *2*.
(37) Ishii, A.; Miyasaka, T. Direct detection of circular polarized light in helical 1D perovskite-based photodiode. *Sci. Adv.* **2020,** *6*, eabd3274.
(38) Dong, Y.; Zhang, Y.; Li, X.; Feng, Y.; Zhang, H.; Xu, J. Chiral Perovskites: Promising Materials toward Next-Generation Optoelectronics. *Small* **2019,** *15*, 1902237.
(39) Nia, N. Y.; Giordano, F.; Zendehdel, M.; Cina, L.; Palma, A. L.; Medaglia, P. G.; Zakeeruddin, S. M.; Gratzel, M.; Di Carlo, A. Solution-based heteroepitaxial growth of stable mixed cation/anion hybrid perovskite thin film under ambient condition via a scalable crystal engineering approach. *Nano Energy* **2020,** *69*, 104411.
(40) Zhang, W.; Sui, Y.; Kou, B.; Peng, Y.; Wu, Z.; Luo, J. Large-Area Exfoliated Lead-Free Perovskite-Derivative Single-Crystalline Membrane for Flexible Low-Defect Photodetectors. *ACS Appl. Mater. Interfaces* **2020,** *12*, 9141-9149.
(41) Mak, K. F.; He, K. L.; Shan, J.; Heinz, T. F. Control of valley polarization in monolayer MoSValley polarization in MoS_2 monolayers by optical helicity. *Nat. Nanotechnol.* **2012,** *7*, 494-498.
(42) Zeng, H. L.; Dai, J. F.; Yao, W.; Xiao, D.; Cui, X. D. Valley polarization in MoS2 monolayers by optical pumping. *Nat. Nanotechnol.* **2012,** *7*, 490-493.
(43) Li, D.; Liu, X. T.; Wu, W. T.; Peng, Y.; Zhao, S. G.; Li, L. N.; Hong, M. C.; Luo, J. H. Chiral Lead-Free Hybrid Perovskites for Self-Powered Circularly Polarized Light Detection. *Angew. Chem. Int. Ed. Engl.* **2021,** *60*, 8415-8418.
(44) Chen, Y.; Ma, J.; Liu, Z.; Li, J.; Duan, X.; Li, D. Manipulation of Valley Pseudospin by Selective Spin Injection in Chiral Two-Dimensional Perovskite/Monolayer Transition Metal Dichalcogenide Heterostructures. *ACS Nano* **2020,** *14*, 15154-15160.
(45) Fang, F. E.; Li, H. N.; Fang, S. F.; Zhou, B.; Huang, F.; Ma, C.; Wan, Y.; Jiang, S. C.; Wang, Y.; Tian, B. B.; Shi, Y. M. 2D $Cs_2AgBiBr_6$ with Boosted Light-Matter Interaction for High-Performance Photodetectors. *Adv. Opt. Mater.* **2021,** *9*, 2001930.
(46) Wang, L.; Xue, Y.; Cui, M.; Huang, Y.; Xu, H.; Qin, C.; Yang, J.; Dai, H.; Yuan, M. A Chiral Reduced-Dimension Perovskite for an Efficient Flexible Circularly Polarized Light Photodetector. *Angew. Chem. Int. Ed. Engl.* **2020,** *59*, 6442-6450.
(47) Peng, Y.; Liu, X. T.; Li, L. N.; Yao, Y. P.; Ye, H.; Shang, X. Y.; Chen, X. Y.; Luo, J. H. Realization of vis-NIR Dual-Modal Circularly Polarized Light Detection in Chiral Perovskite Bulk Crystals. *J. Am. Chem. Soc.* **2021,** *143*, 14077-14082.
(48) Zhang, X. Y.; Liu, X. T.; Li, L. N.; Ji, C. M.; Yao, Y. P.; Luo, J. H. Great Amplification of Circular Polarization Sensitivity via Heterostructure Engineering of a Chiral Two-Dimensional Hybrid

Perovskite Crystal with a Three-Dimensional $MAPbI_3$ Crystal. *ACS Cent. Sci.* **2021,** *7*, 1261-1268.

Graphical Abstract